Cloud height measurement by a network of all-sky-imagers

Niklas Benedikt Blum[1,2], Bijan Nouri[1], Stefan Wilbert[1], Thomas Schmidt[2], Ontje Lünsdorf[2], Jonas Stührenberg[2], Detlev Heinemann[2], Andreas Kazantzidis[3], and Robert Pitz-Paal[4]

[1]Deutsches Zentrum für Luft- und Raumfahrt (DLR), Institut für Solarforschung, Paseo de Almería, 73, 2, E-04001 Almeria, Spain
[2]Deutsches Zentrum für Luft- und Raumfahrt (DLR), Institut für Vernetzte Energiesysteme, Carl-von-Ossietzky-Straße 15, 26129 Oldenburg, Germany
[3]Laboratory of Atmospheric Physics, Department of Physics, University of Patras, 26500 Patras, Greece
[4]DLR, Institut für Solarforschung, Linder Höhe, 51147 Köln, Germany

Correspondence: Niklas Blum (niklas.blum@dlr.de)

Abstract. Cloud base height (CBH) is an important parameter for many applications such as aviation, climatology or solar irradiance nowcasting (forecasting for the next seconds to hours ahead). The latter application is of increasing importance to operate distribution grids as well as photovoltaic power plants, energy storage systems and flexible consumers.

To nowcast solar irradiance, systems based on all-sky-imagers (ASIs), cameras monitoring the entire sky dome above their
5   point of installation, have been demonstrated. Accurate knowledge of CBH is required to nowcast the spatial distribution of solar irradiance around the ASI's location at a resolution down to $5\,\mathrm{m}$. Two ASIs located at a distance of usually less than $6\,\mathrm{km}$ can be combined into an ASI-pair to measure CBH. However, the accuracy of such systems is limited. We present and validate a method to measure CBH using a network of ASIs to enhance accuracy. To the best of our knowledge, this is the first method to measure CBH by a network of ASIs which is demonstrated experimentally.

10   In this study, the deviations of 42 ASI-pairs are studied in comparison to a ceilometer and characterized by camera distance. The ASI-pairs are formed from seven ASIs and feature camera distances of $0.8...5.7\,\mathrm{km}$. Each of the 21 ASI-tuples formed from seven ASIs yields two independent ASI-pairs as the ASI used as main and auxiliary camera respectively is swapped. Deviations found are compiled into conditional probabilities telling how probable it is to receive a certain reading of CBH from an ASI-pair given that true CBH takes on some specific value. Based on such statistical knowledge, in the inference the
15   likeliest actual CBH is estimated from the readings of all 42 ASI-pairs.

Based on the validation results, ASI-pairs with small camera distance (especially if $< 1.2\,\mathrm{km}$) are accurate for low clouds (CBH $< 4\,\mathrm{km}$). In contrast, ASI-pairs with camera distance of more than $3\,\mathrm{km}$ provide smaller deviations for greater CBH. No ASI-pair provides most accurate measurements under all conditions. The presented network of ASIs at different distances proves that, under all cloud conditions, the measurements of CBH are more accurate than using a single ASI-pair.

20

1 Introduction

Cloud base height (CBH) has become an important parameter in meteorology that is required, either directly or indirectly, in many applications. CBH is used to validate and improve climate models (Costa-Surós et al., 2013) and numeric weather prediction models (Hogan et al., 2009). In aviation, CBH is important to air traffic controllers (Khlopenkov et al., 2019; Reynolds et al., 2012; Isaac et al., 2014). As clouds are the major cause of variability of the solar resource, they are of special interest for solar power applications. Here, CBH is of interest to forecast the solar resource for the next seconds to hours ahead (nowcasting). All-sky-imager (ASI)-based nowcast methods require cloud top height (CTH) and CBH to calculate the position and extent of cloud shadows on the ground (Nguyen and Kleissl, 2014). In a similar way, satellite-based nowcast methods can profit from accurate knowledge of CBH and CTH (Bieliński, 2020). The statistical relationship between CBH and a cloud's further properties like optical thickness can be exploited to support the generation of such nowcasts (Nouri et al., 2019c). Also, cloud tracking schemes, used in ASI-based nowcasting, require knowledge of CBH to estimate the absolute displacement of clouds over time.

The method to measure CBH, presented in this study, is used as part of an ASI-based nowcasting system of the solar resource. Such nowcasts can reduce the uncertainty of supply from solar power plants and can support efficient balancing of energy supply and demand (Law et al., 2014; Kaur et al., 2016). The coordination of renewable production and energy consumption at a local scale is a way to minimize requirements on grid-infrastructure while keeping curtailment of feed-ins from renewable sources at a low level. Ghosh et al. (2016) use nowcasts (15 s ahead) to control PV-feed in and provide reactive power. In this context, spatially and temporally highly resolved nowcasts enable distribution grid operators, microgrid controllers and energy management administrators to control backup power, energy storage and flexible consumers. Cirés et al. (2019) pointed out the potential of nowcasts to reduce battery storage capacities required by PV plants under ramp rate restrictions. As implied above, high quality and real time information of local CBH is required at all sites for which accurate nowcasts should be provided.

CBH is commonly measured by ceilometers or other LiDARs. In Germany, the meteorological service Deutscher Wetterdienst (DWD) operates a network of ceilometers which has a distance between stations of approximately $60\,\mathrm{km}$ in the region of the measurement site Oldenburg (Chan et al., 2018). Ceilometers are specialized instruments that come at a high price and provide CBH zenith-wise for the location of their installation. Therefore, we do not consider ceilometers as an option to provide CBH in real time for most solar power plants or cities with many roof top installations. Further, common approaches to measure CBH could be applied for operational use in nowcasting. Among others, these include weather balloons and the estimation of CBH based on a recognized cloud genus (World Meteorological Organization, 2018). Satellites can measure CTH of the highest cloud layer (Hamann et al., 2014) but require estimations of cloud vertical extent (see e.g. Noh et al., 2017) to provide cloud base height (CBH). ASIs can directly measure CBH but require estimations of cloud vertical extent if CTH is of interest. This approach is especially reasonable if ASIs are used at a site for further purposes such as ASI-based nowcasting. ASI-based nowcasting is typically applied if variations of irradiance have to be predicted for lead times immediately ahead ($0...20\,\mathrm{min}$) and at highest temporal and spatial resolution (e.g. $30\,\mathrm{s}$ and $5\,\mathrm{m}$ respectively as used by Nouri et al., 2019b).

ASI-based estimation of CBH may follow different principles. Some approaches first measure the angular velocity of clouds
55 in the sky-image of a single ASI and estimate CBH with an external source of cloud velocity. Wang et al. (2016) derives cloud
velocity by three photocells placed at known distances from each other. Kuhn et al. (2018b) measures cloud velocity by a
cloud speed sensor based on nine photocells and by a shadow camera system and compares the accuracy of received CBH.
Tomographic reconstruction approaches (Mejia et al., 2018) or similarly voxel carving approaches (Nouri et al., 2018) first
model 3-dimensional representations of clouds from which their base height can be retrieved. Stereoscopic approaches match
60 features found in the images of two ASIs. Used ASIs are located in proximity to each other, this way forming an ASI-pair. From
the position of matched features in both images, CBH is triangulated. The literature describes various image features which
can be utilized for this task. Blanc et al. (2017) exploits gradients of intensity. Allmen and Kegelmeyer Jr (1996) used local
velocity in an image point derived by optical flow. Similarly, Savoy et al. (2016) utilized three-dimensional scene-flow making
use of the slow evolution of cloud structures. Kuhn et al. (2018b) subtract red-channel images taken with a temporal offset of
65 30 s and match image areas with the most significant changes. Features from the images of both cameras are typically matched
by block-wise cross-correlation while the used block size may vary between the approaches. Beekmans et al. (2016) generated
dense 3-D representations of cumulus clouds using semi-global block-matching with a very fine block size of 11×11 pixels.
Image areas, for which features are retrieved, are often restricted to areas that are segmented as cloud in a prior step (e.g. Blanc
et al., 2017; Peng et al., 2015). The stereoscopic approach utilized here (Nouri et al., 2019a) enhances the approach by Kuhn
70 et al. (2018b) and works completely independently from cloud recognition which is considered to bring a greater robustness.

Most ASI-systems described in the literature feature one (Schmidt et al., 2016), two (Allmen and Kegelmeyer Jr, 1996;
Beekmans et al., 2016; Blanc et al., 2017; Savoy et al., 2016) or three (Peng et al., 2015) ASIs. Four ASIs have been used by
(Kuhn et al., 2018a; Nouri et al., 2019a) and such systems are available at four different sites (Nouri et al., 2019b). A network
of six ASIs accompanied the HOPE measurement-campaign in 2013 around Jülich, Germany (Macke et al., 2017). In the city
75 state of Singapore, a larger number of 16 ASIs, interacting in a network to monitor the sky and clouds (in the following referred
to as ASI network), has been set up (Sky cameras, 2020). A method to monitor clouds with an ASI network using tomographic
reconstruction has been described conceptually and based on synthetic data by Mejia et al. (2018). Aides et al. (2020) studied a
similar approach experimentally using an actual ASI network of up to 14 cameras located in an area of $12 \text{ km} \times 12 \text{ km}$ around
Haifa, Israel. ASI-networks have additionally been reported in astronomy, to track meteorites during nighttime (Howie et al.,
80 2017).

In this study, seven of the ASIs included in the Eye2Sky ASI network (Schmidt et al., 2019; Blum et al., 2019a, b) are used.
The selected ASIs are located in the city of Oldenburg. At the moment of writing, Eye2Sky contains 24 ASIs in Oldenburg
and a region of about $110 \text{ km} \times 100 \text{ km}$ to the west of Oldenburg. An approach is presented to measure CBH by the ASI
network that allows the use of multiple ASI-pairs in proximity simultaneously. 42 ASI-pairs are formed from the seven ASIs
85 and CBH is estimated by each ASI-pair based on the method presented by Nouri et al. (2019a). In a period of three months,
the accuracy of the included ASI-pairs is evaluated for distinct conditions. Gained knowledge about the deviations of each
ASI-pair is applied to merge the measurements of CBH from all 42 ASI-pairs into a more reliable measurement.
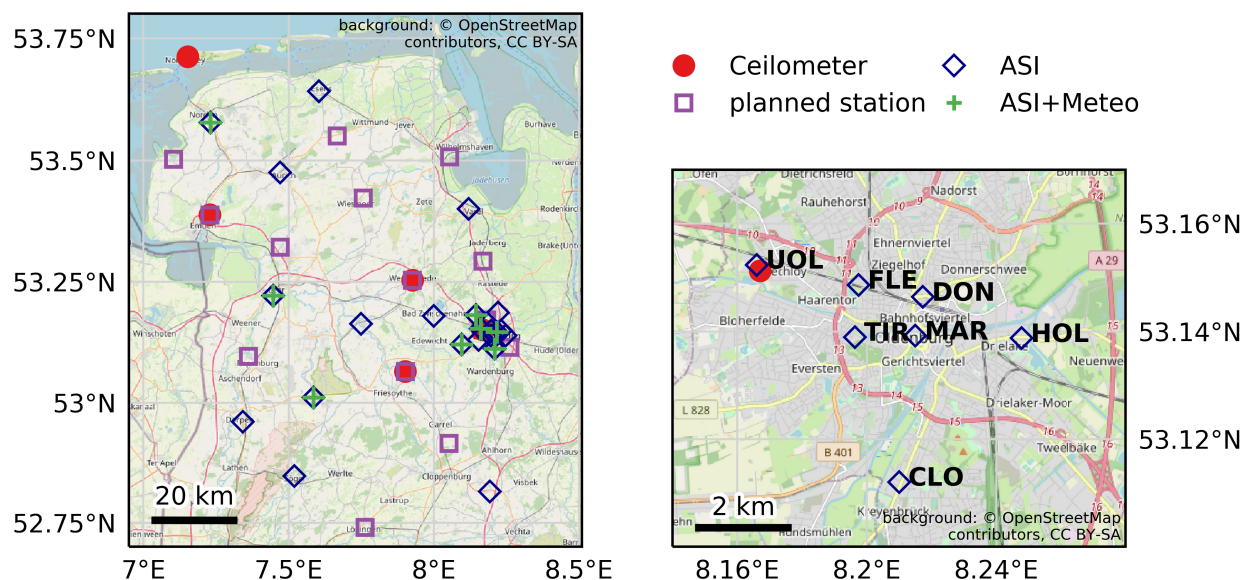
Atmospheric
Measurement
Techniques

Open Access

EGU

Discussions

Figure 1. Overview of the Eye2Sky ASI network including operational ASIs (ASI), radiometric measurements (Meteo) as well as planned stations (left) and ASIs in the city of Oldenburg included in this study (right). The ceilometer used as reference (marked by a red circle in the right figure) is located near the northwest-most ASI UOL. (background: © OpenStreetMap contributors 2020. Distributed under a Creative Commons BY-SA License.)

This publication is structured as follows. First, Eye2Sky, the ASI network used in the experiments, is introduced (Sect. 2). Then, the measurement procedure of CBH using the ASI network is presented (Sect. 3). Here, the properties of CBH measured by reference ceilometer and by 42 ASI-pairs are discussed (Sect. 3.1). The meteorological conditions at the site are studied next (Sect. 3.2). In Sect. 3.3 and Sect. 3.4, a novel procedure to combine CBH measurements from multiple ASI-pairs of the ASI network is presented. Section 4 analyzes CBH measurement by the ASI network in comparison to the individual ASI-pairs for all relevant conditions. A summary of the presented findings closes the study in Sect. 5.

2   Eye2Sky network and experimental setup

The so called Eye2Sky ASI network is being set up in the region of Oldenburg (Fig. 1, left). At its full extent, Eye2Sky will include 38 stations distributed over an area of roughly $110 \, \text{km} \times 100 \, \text{km}$ equipped with ASIs. 13 of these stations will be supported by additional meteorological measurements to provide beam, diffuse and global irradiance via rotating shadowband irradiometers as well as ambient temperature and relative humidity. Eight ceilometers will be included in the network. Six of
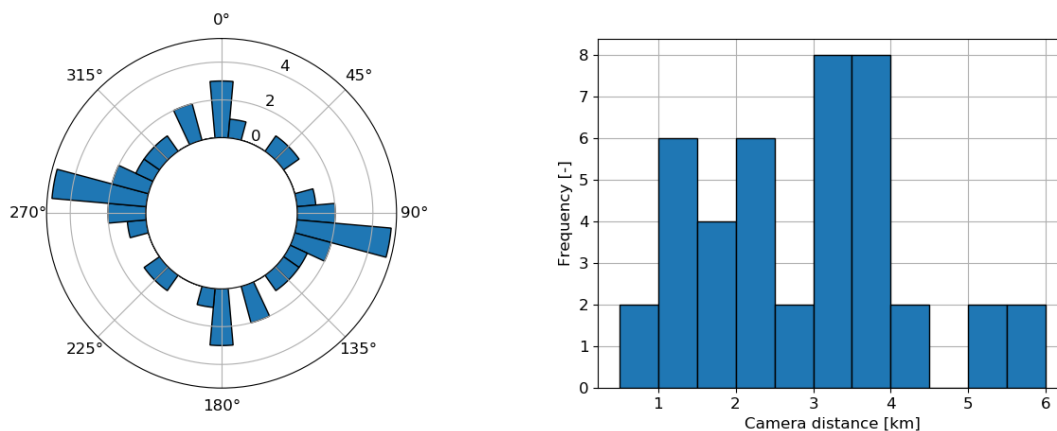
Figure 2. Frequency distribution of camera axis bearing angles in the set of available ASI-pairs (over north, left) and of available camera distances (right) resulting when arranging the seven ASIs in the urban area into 42 ASI-pairs (from each ASI-tuple two different ASI-pairs result by switching the main camera)

these are operated by the meteorological service Deutscher Wetterdienst (DWD). Five of these ceilometers are in the region
100 viewed in Fig. 1. Several PV plants and numerous smaller distributed PV installations are also present in the study area. With
its regional coverage, Eye2Sky aims to achieve nowcasts for individual PV installations from some minutes to multiple hours
ahead. In the urban area of Oldenburg, the network will feature a high density of 14 ASIs in an area of $13 \, \text{km} \times 12 \, \text{km}$. This
dense setup aims to provide ASI-based nowcasts of high accuracy across the urban area and reliable estimation of CBH under
all conditions is an important contribution to achieve this scope.

105   This work utilizes seven ASIs and one ceilometer located in the city of Oldenburg (Fig. 1, right). The ceilometer is located
$133 \, \text{m}$ southeast of to the most northwestern ASI UOL. All included ASIs except for UOL are located east and south of the
ceilometer. ASIs are placed at most $5.7 \, \text{km}$ from this ceilometer. For this study, these ASIs are arranged into several ASI-pairs
as defined by arbitrarily selecting a tuple of ASIs (21 tuples are available) and forming two independent ASI-pairs from each
tuple by swapping its main camera. The main camera of an ASI-pair is central to the measurement of CBH through an ASI-pair,
110 described in more detail in Sect. 3.1, and defines the center of the area for which CBH is estimated. From 21 ASI-tuples, 42
ASI-pairs are received. The paired cameras' distance and the orientation of the camera axis characterize the ASI-pairs. The
orientation of a camera axis is defined as seen from the main ASI and given in degree north. Figure 2 shows the distribution
of orientations of camera axes (left) and camera distances (right) in the set of available ASI-pairs. This set covers almost all
possible orientations of camera axes. Available camera distances $0.8...5.7 \, \text{km}$ cover most of the range $0.02...5.5 \, \text{km}$ that is used
115 in literature (Kuhn et al., 2019). Only towards small camera distances below $0.8 \, \text{km}$, the present set lacks further ASI-pairs.

The used ceilometer is of type Lufft CHM 15 k Nimbus. The used ASIs are surveillance cameras of type Mobotix Q25 with
a fisheye lens providing $180°$ field of view. The ASIs are configured to use a constant exposure time of $149 \, \text{µs}$ and a constant
color temperature of $5500 \, \text{K}$. The effective image resolution is $2048 \, \text{pixel} \times 2112 \, \text{pixel}$. An exemplary sky image from ASI

UOL is shown in Fig. 3, left. The ASIs' intrinsic calibration was determined according to Scaramuzza et al. (2006). The ASIs'
locations defined by latitude, longitude and altitude were identified in geolocated satellite images. Altitude was estimated based
on the local altitude of the ground and the stations' height over ground. The exact orientation of the ASIs' field of view was
computed from the trajectory of the full moon registered in nighttime images as described by Nouri et al. (2019a).

The ASIs provide sky images at every half and full minute. The ceilometer provides readings $0, 15, 30, 45$ s after each full
minute. The clock of each measurement instrument is at any time synchronized via NTP (Network Time Protocol). Sky images,
measurements of CBH and meteorological parameters are uploaded over the cellular network to a central server typically within
2.5 s and in most cases within 5 s after acquisition. A high-performance computer (HPC) is used to compute CBH from sky
images. Image processing takes up the major share of the computation time required by the presented method. These tasks are
performed in parallel for each of the seven ASIs (typically allocating 4 CPUs of 3.4 GHz and 1 GB memory to each ASI)
avoiding redundant calculations. In this way, computational cost scales mostly linear with the number of ASIs used instead of
with the number of ASI combinations so that execution in real time is possible.

The dataset used in this study covers the period from 01 April 2019 through 27 September 2019. It is split into a period used
for deriving the method (until 29 June 2019) and a period used for validations (starting from 30 June 2019).

3   Development of a CBH estimation using the ASI network

In this section we present a procedure to estimate CBH by an ASI network. The procedure aims to be more accurate compared
to an estimation of CBH by independent ASI-pairs. First, properties of the reference CBH received from a ceilometer and
properties of CBH received from ASI-pairs are discussed. Next, meteorological conditions at the site are discussed which are
relevant to the performance of a CBH measurement. Based on this, we develop the estimation which borrows principles from
Maximum Likelihood Estimation (MLE).

3.1   Properties of CBH measurements from ceilometers and from ASI-pairs

As introduced in Sect. 2, a ceilometer of type Lufft CHM 15 k Nimbus is used as reference in the development and validation
presented in this study. When low and thick clouds are present, only the lowest cloud layer is expected to be recognized reliably
by the ceilometer and readings provided for overlaid cloud layers are not evaluated. Regarding the accuracy of the instrument,
a benchmark by Martucci et al. (2010) exhibited a bias of the instrument compared to another manufacturer's ceilometer of
160 m. With this in mind, we still consider the instrument to be sufficiently accurate for the scope of this study.

From all ASIs available in the urban area, we form independent ASI-pairs that measure CBH by a stereoscopic triangulation
method. The method used here was introduced by Kuhn et al. (2018b) and further refined by Nouri et al. (2019a). Images from
both cameras are first projected into horizontal planes yielding orthogonal images by a well established method described e.g.
by Luhmann (2000). Then, the difference in the red-channel of consecutive images is calculated for each camera. Areas in
the difference images of the two cameras, in which the red-channel changes most significantly (98-percentile) within the 30 s
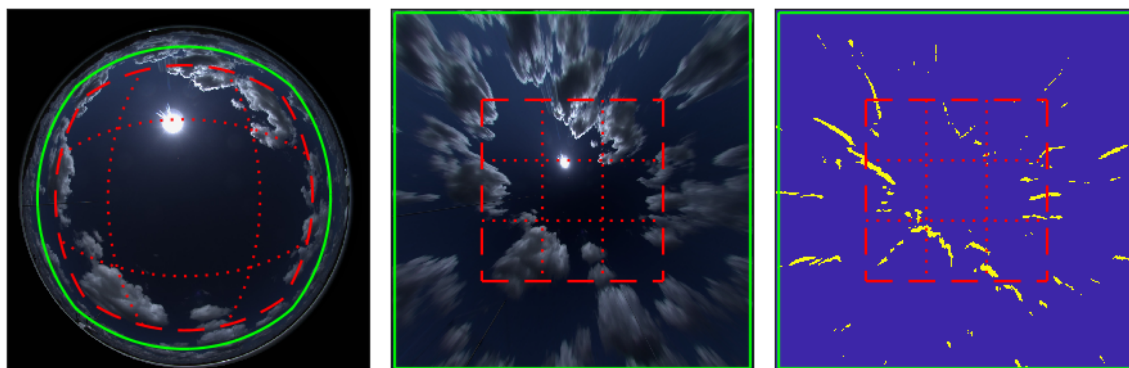
Figure 3. Sky area (exemplary at UOL) evaluated in the measurement of CBH. Maximum extent (solid green shape) and area used by the main camera in the default case (red dashed shape) in the distorted ASI image (left), in the undistorted ortho-image (center), in the binary red-channel difference image of two consecutive exposures (right). The binary red-channel difference image (right) shows areas considered as features in the cross-correlation for the comparison to the second camera as yellow shapes.

150   between consecutive images, are used as features (illustrated in Fig. 3, right) to be matched by block-wise correlation. With the known camera distance, a shift received in cross-correlation is translated into a height of the feature over ground.

In practice, the triangulation relies on cloud edges which are visible from both perspectives and provide sufficient contrast. Therefore, the method responds stronger to optically dense clouds, especially in the proximity of the sun (Kuhn et al., 2018b). Moreover, we do not exactly measure CBH but the height of these distinct cloud edges. We expect to introduce a small bias

155   when using this cloud height as CBH. Nouri et al. (2019a) analyzed sources of deviations when estimating CBH by an ASI-pair. In accordance with that study, we expect this bias to be acceptable compared to other uncertainties and to be in the order of 100 m.

In the present study, we use a cascading procedure to estimate CBH robustly also in conditions with low sky coverage. We first project the field of view of each camera up to a maximum zenith angle of $67°$, measured at the center of each image side,

160   into an orthoimage of square shape (Fig. 3, red dashed shape). In the correlation, the central area (or window, Fig. 3, central red dotted box) from the orthoimage of the main camera is matched with a window of identical dimensions from the orthoimage of the second camera. This central window of the orthoimage of the main camera covers zenith angles up to $38.1°$, measured at the center of each window side. Therefore, a CBH measurement for a square-shaped area around the main camera's location is yielded. For example, the area's side lengths measure $1.6, 4.7, 7.8, 15.7$ km for a respective CBH of $1, 3, 5, 10$ km.

165   If the estimation of CBH fails for this central window, we use the CBH that is measured by matching the peripheral windows (Fig. 3, peripheral red dotted boxes) of the same orthoimage with the orthoimage of the second camera. These peripheral windows of an orthoimage have the same shape as the central window (see Fig. 3, center, peripheral red dotted boxes). If a valid estimation of CBH is received for multiple peripheral windows, we use the average CBH from these windows.

For cases with still no valid measurement, images of both cameras are evaluated up to a maximum zenith angle of $77.8°$

170   (measured at the center of each image side). These image areas are projected into orthoimages (green shapes in Fig. 3).
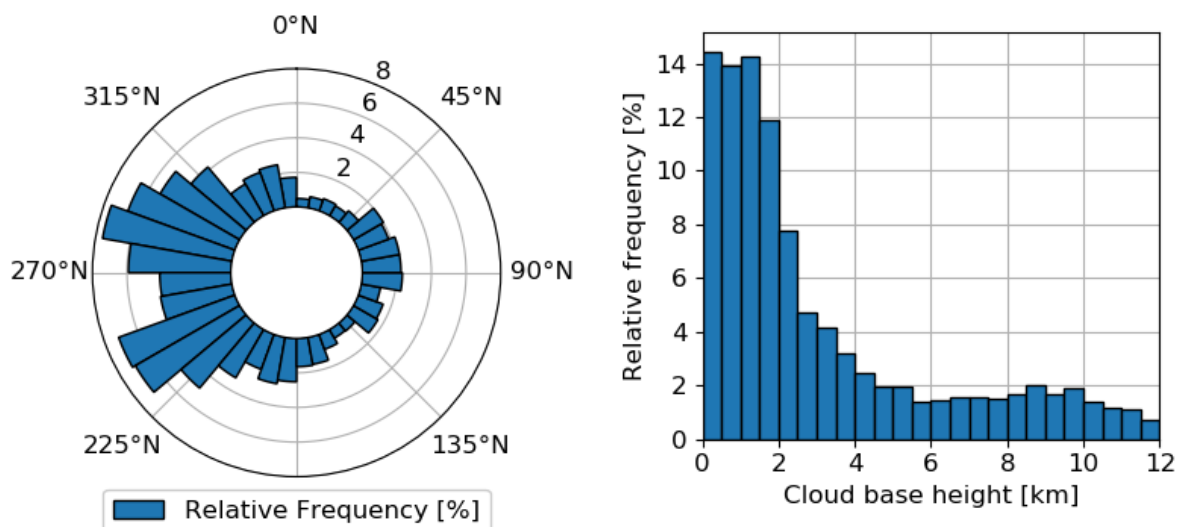
Figure 4. Wind rose of cloud motion directions derived from UOL camera indicating a dominance of clouds coming from western directions (left) and distribution of cloud base height (CBH) in the analyzed period (right)

Resulting orthoimages from both cameras are matched in the cross-correlation. Overall, we expect that, by applying cross-correlation to binary difference images, our measurement approximates the median CBH of the cloud layer that is locally most dominant in the sense of area and optical thickness.

A previous study by Kuhn et al. (2019) showed that camera distance and CBH itself significantly influence the accuracy received in the measurement of CBH by an ASI-pair with the present approach. Based on this, we use camera distance and CBH to characterize ASI-pairs.

3.2 Meteorological conditions at the site

To understand the performance of the CBH measurement based on ASI-pairs we briefly analyze the meteorological conditions on-site based on ceilometer and ASI data. Using ASI UOL we study the dominant directions of cloud motion at the site. Nouri et al. (2019a) found a root mean squared deviation (RMSD) of $17°$ for the estimation of the direction of cloud motion based on an ASI-pair. Based on this, we consider the estimation of cloud motion directions from ASI UOL as sufficiently accurate for this statistical evaluation. Figure 4 left shows the distribution of cloud motion directions estimated with the ASI in the sense of a wind rose representing the directions from which clouds approach the urban area. Two main lobes at azimuthal angles of $240°N$ (west to south-west) and $290°N$ (west to north-west) are seen while other directions of cloud motion are observed rather seldom.

The distribution of CBH at the site of Oldenburg for the full measuring period is given in Fig. 4 right. The majority of all ceilometer readings (54 %) indicates a CBH smaller than 2 km. Within the interval CBH $\in]0,2[$ km all values are observed similarly frequent. This includes the lowest bin of CBH $\in]0,0.5[$ km which indicates conditions with fog or low stratus clouds.

Atmospheric
Measurement
Techniques
Open Access
EGU
Discussions

For the majority of situations, it is of special interest to receive accurate measurements in the low range of CBH. Moreover,
190   28% and 18% of readings are found respectively in the intermediate range of CBH $\in [2,6[$ km and in the range of large
CBH $\in [6,12[$ km. Within the range of high clouds, a roll-off of the frequency is seen for CBH > 10 km. A reliable estimation
of CBH should therefore provide accurate readings for the range of CBH $\in]0,12[$ km.

A visual analysis and a k-means classification for the site of Oldenburg suggested that local conditions predominantly feature
distinct cloud layers with temporally low vertical variability. The major cause of variable CBH is found in the transitions
195   between cloud layers. It is concluded that for sites with similar meteorological conditions, it is most important to measure
CBH of the cloud layer which is most dominant at the evaluated time as accurately as possible. Kottek et al. (2006) characterize
the climate in Oldenburg as warm temperate, fully humid with warm summers (Cfb). In this publication a summer half-year
period (April...September) is studied. The climate is strongly influenced by the North Sea which is located at a distance of
roughly 70 km. Eye2Sky and especially Oldenburg are situated in a plane with a maximum elevation over sea level of less
200   than 160 m including vegetation and human infrastructure (TanDEM-X topographic data used in this study is described by
Wessel et al., 2018). The flat topography is expected to support a temporally and spatially low variability of CBH within cloud
layers. For other sites, a focus on measuring CBH for every cloud object is of higher priority. Tabernas, the site studied by
Nouri et al. (2019a), features a cold-arid steppe climate (BSk according to Kottek et al., 2006) and is surrounded by mountains
with elevations up to 2168 m over sea level within a radius of 25 km. As shown by (Nouri et al., 2019c), CBH at the site
205   is distributed almost uniform in the range 0...11 km. These characteristics are expected to cause greater temporal and spatial
variability of CBH.

3.3 Estimation of conditional probabilities of CBH

The procedure to combine CBH-measurements from independent ASI-pairs, which are organized as a network, requires knowl-
edge of the (conditional) probability to receive a certain reading of CBH from an ASI-pair given the true CBH takes on some
210   specific value. The method itself will be presented in Sect. 3.4. Here we discuss the probability distributions used. The required
distribution aims to answer the following question: If true CBH ranges in between 1.8...1.9 km, how large will be the probabil-
ity that an ASI-pair with camera distance 2.2 km delivers a certain CBH e.g. within 0...0.1 km or 1.8...1.9 km or 11.9...12 km?
In the following, these conditional probabilities are estimated not only for the range of true CBH between 1.8...1.9 km but for
each range $\{0...0.1, 0.1...0.2, 0.2...0.3, ..., 11.9...12\}$ km of true CBH. Estimations of CBH from the available ASI-pairs and
215   measurements from the ceilometer during the period 01 April 2019 to 29 June 2019 are used. CBH measured by the ceilometer
serves as reference CBH.

The seven ASIs available in the urban area are arranged into 42 ASI-pairs. Each tuple of ASIs, that is selected from the set
of seven ASIs, yields 2 independent ASI-pairs by swapping the ASI used as main camera (see Sect. 3.1).

The procedure is developed based on periods in which valid measurements from ceilometer and the respective ASI-pair are
220   available and in which the variability of CBH is moderate: For each time stamp a window of 30 min centered at this time
stamp is defined. A time stamp is only included if standard deviation of reference CBH within the window is less than 30%
of the mean value of reference CBH within the same window. As discussed before, ASI-pairs and ceilometer measure CBH as

Atmospheric
Measurement
Techniques
Discussions
Open Access
EGU

spatial median and point-wise respectively. Therefore, this filter intends to assure that ceilometer and ASI-pair measure CBH of the same layer. CBH from the respective ASI-pair and from the ceilometer are processed by a moving-median filter with a window of $10 \, \mathrm{min}$. The joint frequency distribution of CBH measured by ceilometer h_{Ref} and the respective ASI-pair h_{ASI} is computed from these simultaneously acquired time series. That means the frequency is calculated with which (h_{Ref}, h_{ASI}) is observed in a discrete grid cell defined by the interval $[j\Delta h, (j+1)\Delta h[$ for h_{Ref} and the interval $[k\Delta h, (k+1)\Delta h[$ for h_{ASI}, where $j, k \in \{0, 1, 2, ..., N-1\}$. A bin size $\Delta h = 100 \, \mathrm{m}$ is chosen in a trade-off between sources of error. Finer bins will allow to represent the distributions at higher resolution and will thus allow for higher resolved measurements of CBH in the network. However, the size of the used data set is limited which makes it difficult to model these distributions at highest resolution. The bin size chosen here is expected to limit the achievable uncertainty of the measurement to a minimum level of $100 \, \mathrm{m}$. Joint frequency distributions modeled here are restricted to a maximum CBH of $12 \, \mathrm{km}$. This yields $N = 120$.

Joint frequency distributions were inspected and found to be well reproduced among the studied independent ASI-pairs, if only the corresponding camera distances are similar. This meets the expectation from literature discussed in Sect. 3.1. Moreover, we conclude that the distributions modeled here will be transferable to other setups that use camera distances in the studied range. Local climate is expected to influence the transferability to a minor extent as will be discussed later. To further support this transferability to other setups, sites and times, we aim to suppress random features of received joint frequency distributions. For this, the original joint frequency distribution F_l of ASI-pair l is transformed by a first filter into $F_{l, filter\ 1}$ and by a consecutively applied filter into $F_{l, filter\ 2}$. First, a weighted mean filter is applied between joint frequency distributions F_l received from all ASI-pairs with arbitrary camera distance d

$$F_{l, filter\ 1} = \frac{\sum_j w_{l,m} F_m}{\sum_j w_{l,m}}. \tag{1}$$

For the joint frequency distribution F_l of each respective ASI-pair l, weights $w_{l,m}$ are used that include ASI-pairs with similar camera distance. More precisely, a triangular window, based on the difference of camera distance $\Delta d_{l,m}$ of ASI-pair m compared to ASI-pair l, is used that is defined by

$$w_{l,m} = max(0, 1 - \Delta d_{l,m}/0.5 \, \mathrm{km}). \tag{2}$$

Then a composite of three Gaussian filters is applied to $F_{l, filter\ 1}$ of each ASI-pair l. We first decompose each distribution $F_{l, filter\ 1}$ by conditional filters into three separate *modes*. In the second step, we apply to each mode a Gaussian filter g_σ with distinct standard deviation σ_{mode} of the Gaussian kernel. The subscript *mode* indicates the specific mode for which σ_{mode} is applied. The first mode is constituted by all outlier observations. Outliers are defined here as grid cells (h_{Ref}, h_{ASI}) for which ASI-pair measurement of CBH h_{ASI} deviates by more than $1.5 \, \mathrm{km}$ from the ceilometer reading h_{Ref}:

$$F_{l, outlier}(h_{Ref}, h_{ASI}) = \begin{cases} F_{l, filter\ 1}(h_{Ref}, h_{ASI}), & |h_{ASI} - h_{Ref}| > 1.5 \, \mathrm{km} \\ 0, & \text{else.} \end{cases} \tag{3}$$

Such outliers will contain a large random component. We expect that in a reproduction of the experiment, a similar number of outliers will be received, while the joint frequency found for a single grid cell (h_{Ref}, h_{ASI}) may vary significantly. Therefore, the strongest filter is applied to this mode using $\sigma_{outlier} = 1 \, \mathrm{km}$.

Atmospheric
Measurement
Techniques
Discussions

Open Access

EGU

The second mode is constituted by grid cells that are not part of the first mode and feature a joint frequency less than the average over all grid cells of the joint frequency distribution:

$$
F_{l,inconfident}(h_{Ref}, h_{ASI}) = \begin{cases} F_{l,filter\ 1}(h_{Ref}, h_{ASI}), & |h_{ASI} - h_{Ref}| \leq 1.5 \text{ km} \\ & \wedge\ F_{l,filter\ 1}(h_{Ref}, h_{ASI}) < \text{mean}(F_{l,filter\ 1}) \\ 0, & \text{else.} \end{cases}
\tag{4}
$$

The comparably small number of observations in these grid cells is expected to cause an increased uncertainty of the estimated joint frequencies. For this mode, $\sigma_{inconfident} = 0.5$ km is applied.

The third mode $F_{l,confident}(h_{Ref}, h_{ASI})$ makes up the complementary of the first and second mode. It contains grid cells that are observed with an at least average joint frequency and which are not classified as outliers:

$$
F_{l,confident}(h_{Ref}, h_{ASI}) = \begin{cases} F_{l,filter\ 1}(h_{Ref}, h_{ASI}), & |h_{ASI} - h_{Ref}| \leq 1.5 \text{ km} \\ & \wedge\ F_{l,filter\ 1}(h_{Ref}, h_{ASI}) \geq \text{mean}(F_{l,filter\ 1}) \\ 0, & \text{else.} \end{cases}
\tag{5}
$$

Joint frequencies in these grid cells are considered to have a comparably high accuracy. To avoid a loss of precision and ultimately a loss of accuracy in the estimation of CBH, a small value of $\sigma_{confident} = 0.1$ km is used. The three filtered modes g_σ are summed to receive the smoothened joint frequency distribution

$$
F_{l,filter\ 2} = g_{\sigma_{outlier}}(F_{l,outlier}) + g_{\sigma_{inconfident}}(F_{l,inconfident}) + g_{\sigma_{confident}}(F_{l,confident}).
\tag{6}
$$

In many joint frequency distributions, there are grid cells with joint frequency close to zero. Especially for these grid cells, a greater dataset would be required to receive more representative values. For all grid cells, joint frequency is increased to a minimum value of 0.5 to avoid underestimations of joint frequency. For the estimation procedure of CBH, this leads to slightly reduced precision for most readings but increased robustness in the case that these grid cells (h_{Ref}, h_{ASI}) are indeed observed in the measurement.

Finally, each joint frequency distribution is normalized with the sum of all joint frequency grid cells. In this way, a probability mass function (also known as discrete density function) to measure a certain CBH with the respective ASI-pair and to coincidentally measure a certain CBH with the ceilometer is yielded. The conditional probability $P(h_{ASI} \mid h_{Ref})$ to receive a certain CBH reading from an ASI-pair, given that the ceilometer measures some certain CBH, is calculated by dividing the respective probability mass function by the marginal distribution of CBH measured by the ceilometer. The latter distribution gives the probability to receive CBH from the ceilometer within a certain bin h_{Ref} regardless of which CBH reading is simultaneously received from an ASI-pair. The distrbution can be derived from any of the probability mass functions by summing all grid cells of the probability mass function which correspond to the respective bin h_{Ref} of CBH measured by the ceilometer.

The inference procedure, which is introduced in Sect. 3.4, represents each range i of camera distance bounded by the limits $\{0.5, 1, 1.5, ..., 6\}$ km by a single distribution of conditional probability. For each range of camera distance, the distribution of conditional probability, which corresponds to the camera distance closest to the center of this range, is selected. For example,
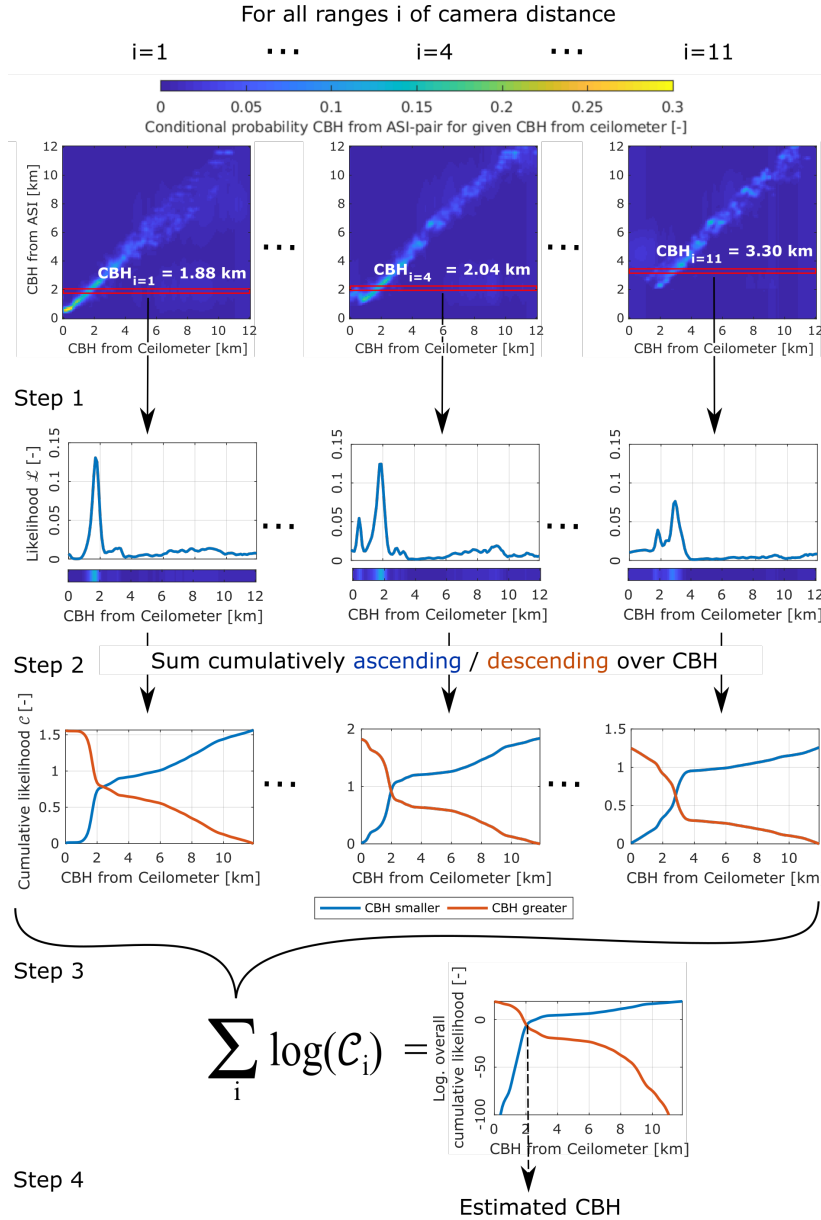
Figure 5. Inference procedure — Step 1: For each range i of camera distance CBH_i is computed as mean CBH from the respective ASI-pairs. Conditional probability is evaluated that CBH_i would be received if true CBH (at the ceilometer) took on a value $\{0...0.1, 0.1...0.2, ..., 11.9...12\}$ km (red boxes). Step 1 yields a likelihood function for each range of camera distance. Step 2: Cumulative and complementary cumulative likelihood are calculated for each range of camera distance. Step 3: These functions are logarithmized and then summed over all ranges i of camera distance yielding overall cumulative and complementary cumulative likelihood. Step 4: The Intersection of both functions gives the estimated likeliest CBH.

for the range $i = 2$ representing camera distances $1...1.5$ km, the center of the range would be 1.25 km. For the camera distances 1.081, 1.247 and 1.352 km, conditional probabilities have been modeled. Consequently, for this range of camera

285 distance, the distribution of conditional probability corresponding to the camera distance 1.247 km is used. Figure 5 (above Step 1) shows exemplary conditional probabilities for three ASI-pairs with camera distances 0.8, 2.2, 5.7 km representing the ranges of camera distance $i = 1$, 4, 11 respectively. The further content of Fig. 5 is explained in the next section.

3.4 Estimating CBH in the ASI network

The estimation procedure presented here is motivated by Maximum Likelihood Estimation (MLE). Figure 5 shows the infer-

290 ence process used to estimate CBH by the network based on the 42 CBH readings provided by the individual ASI-pairs. For each range i of camera distance, conditional probabilities estimated in Sect. 3.3, are translated into the likelihood that actually certain values of CBH are present (step 1) based on the readings of CBH received for this range i of camera distance. After calculating the cumulative likelihood for each range of camera distance (step 2), these are combined yielding the overall cumulative and complementary cumulative likelihood from all ASIs (step 3). Finally, the value of CBH which is most likely to be

295 present at the site and at the evaluated time, given the readings from all involved ASI-pairs, is estimated (step 4). These steps are explained in more detail in the following.

Step 1: For each ASI-pair, the median value of all valid CBH readings of the previous 10 min is calculated. If an ASI-pair does not provide any valid CBH within this period, it is excluded from the prediction for the instance in time evaluated. The ranges of camera distance $1...2.5$ km and $3...4$ km are represented by a larger number of ASI-pairs than the remaining

300 distances. To represent all camera distances as uniformly as possible, ranges of camera distance are defined using the range limits $\{0.5, 1, 1.5, ..., 6\}$ km and CBH readings of all ASI-pairs with camera distance in range i are averaged to yield CBH_i. Consecutively, the conditional probability $P(\mathrm{CBH}_i \mid \theta)$ is evaluated that the found CBH_i would be received for a given true CBH θ (red marked box prior to step 1 in Fig. 5). Note that $P(\mathrm{CBH}_i \mid \theta)$ was modeled in Sect. 3.3 measuring CBH h_{Ref} by a ceilometer which provided $h_{Ref} \approx \theta$. Thus, the likelihood $\mathcal{L}_i(\theta)$ is obtained (Fig. 5, output of step 1):

305 $$\mathcal{L}_i(\theta) = P(\mathrm{CBH}_i \mid \theta). \tag{7}$$

Step 2: Likelihood is summed cumulatively over all bins of reference CBH θ to define cumulative likelihood (Fig. 5, step 2):

$$\mathcal{C}_i(\hat{\theta}) = \sum_{\theta \leq \hat{\theta}} \mathcal{L}_i(\theta). \tag{8}$$

Likewise, a complementary cumulative likelihood is defined

$$\bar{\mathcal{C}}_i(\hat{\theta}) = \sum_{\theta > \hat{\theta}} \mathcal{L}_i(\theta). \tag{9}$$

310 $\mathcal{C}_i(\hat{\theta})$ and $\bar{\mathcal{C}}_i(\hat{\theta})$ are used here as measures how likely it is that actual CBH θ is in the interval $]0$ km$, \hat{\theta}]$ or $]\hat{\theta}, 12$ km$]$ respectively. It is mainly the use of these cumulative functions that distinguishes the present approach from a Maximum-Likelihood-Estimation (MLE). This modification is used as in MLE typically smooth analytical likelihood functions are assumed. In

contrast, likelihood functions here are estimated based on empirical conditional probabilities. These approximated likelihood-functions, derived from a dataset of finite size, may therefore be less smooth and may not be completely representable. In

315 spite of the modification, the presented approach may adopt beneficial properties of MLE: The use of appropriate conditional probabilities (described in Sect. 3.3) reduces systematic deviations of estimated CBH compared to the measurement of a single ASI-pair. Moreover, applied conditional probabilities are in general not specific to the studied site and its meteorological conditions which allows to apply the method at other sites. When using cumulative distributions, it is expected that the method still works robustly if the conditional probabilities are not estimated accurately for each joint frequency grid cell but at least the

320 cumulative value over a range of CBH is appropriate. Both functions $\mathcal{C}_i(\hat{\theta})$ and $\bar{\mathcal{C}}_i(\hat{\theta})$ are shown for three exemplary intervals of camera distance in Fig. 5 as output of step 2.

Step 3: The natural logarithm is then applied to $\mathcal{C}_i(\hat{\theta})$ and summed over all intervals i of camera distance to yield the overall logarithmized cumulative likelihood (Fig. 5, step 3) given the readings CBH_i per interval i of camera distance

$$\log \mathcal{C}_n(\hat{\theta}) = \sum_i \log \mathcal{C}_i(\hat{\theta}). \tag{10}$$

325 Analogously, an overall complementary logarithmized cumulative likelihood is computed given all readings CBH_i per interval i of camera distance

$$\log \bar{\mathcal{C}}_n(\hat{\theta}) = \sum_i \log \bar{\mathcal{C}}_i(\hat{\theta}). \tag{11}$$

Both functions are visualized exemplarily as output of step 3 in Fig. 5. In theory, the method could do without the application of a logarithm to $\mathcal{C}_i$ and $\bar{\mathcal{C}}_i$ in Eq. (10) and Eq. (11) respectively. In that case, the sum would be replaced by a multiplication in

330 the respective equations. However, this would induce numerical problems regularly as handled products approach zero.

Step 4: The left hand sides in Eq. (10) and Eq. (11) are only known at discrete points. Linear interpolation yields continuous representations of these. An estimation of the likeliest actual CBH $\theta_{likeliest}$ is selected for which $\log \bar{\mathcal{C}}_n(\hat{\theta})$ and $\log \mathcal{C}_n(\hat{\theta})$ are equal (Fig. 5, step 4)

$$\theta_{likeliest} = \operatorname*{argmin}_{\hat{\theta}} \left| \log \bar{\mathcal{C}}_n(\hat{\theta}) - \log \mathcal{C}_n(\hat{\theta}) \right|. \tag{12}$$

335 Besides this estimation of CBH, a version of this procedure will be discussed that includes further refinements (in the following referred to as *refined* estimation). The refinement is motivated by the finding that some ASI-pairs are already accurate if actually a certain range of CBH is present as we will discuss in Sect. 4. First, the procedure presented above is modified to exclude ASI-pairs with camera distance greater than 4.5 km as these ASI-pairs cause large deviations for $\mathrm{CBH} < 4$ km and only provide a limited benefit at greater CBH. Results from this procedure are accepted as refined estimation $\theta_{refined}$ if

340 estimated CBH is within $3...12$ km. Otherwise, the arithmetic average of CBH measured by ASI-pairs with specific camera distance is used. The most appropriate ASI-pairs for an interval of CBH are identified by an inspection of the conditional probabilities (exemplarily viewed as input to step 1 in Fig. 5). This refined estimation is restricted to remain within the specific interval of CBH from the unrefined estimation in which it is applied. In summary, the refinement procedure to receive the final

Atmospheric
Measurement
Techniques
Discussions

estimation of CBH $\theta_{refined}$ reads

$$
\theta_{refined}
\begin{cases}
\theta_{likeliest}, & \theta_{likeliest} \in\,]3, 12]\ \mathrm{km} \\
\min(3\ \mathrm{km}, \mathrm{mean}(h_{i \in \{i|d_i < 1.6\ \mathrm{km}\}})), & \theta_{likeliest} \leq 3\ \mathrm{km} \wedge \mathrm{mean}(h_{i \in \{i|d_i < 1.6\ \mathrm{km}\}}) > 1.5\ \mathrm{km} \\
\min(1.5\ \mathrm{km}, \mathrm{mean}(h_{i \in \{i|d_i < 1.2\ \mathrm{km}\}})), & \theta_{likeliest} \leq 3\ \mathrm{km} \wedge \mathrm{mean}(h_{i \in \{i|d_i < 1.6\ \mathrm{km}\}}) \leq 1.5\ \mathrm{km}.
\end{cases}
\tag{13}
$$

4   Validation of CBH measurement by the ASI network and comparison to CBH measurements by the ASI-pairs

In this section, the accuracy of CBH measurement by the ASI network and by 42 independent ASI-pairs set up at a wide variety of camera distances and alignments is compared. This section is based on a validation data set including the days from 30 June 2019 to 27 September 2019. The analyzed quantity is $10\ \mathrm{min}$-median CBH. The evaluations are restricted to times in which the variability of CBH is small. More precisely, the standard deviation of CBH within a window $15\ \mathrm{min}$ before and after the analyzed time is required to be less than 30% of mean CBH within the same window. As discussed above, the ASI-pairs and the ASI network are expected to measure a spatial median CBH whereas the ceilometer measures CBH at the point of its installation. This restriction aims to assure comparability of both measurements.

First, characteristics of CBH-measurements from the ASI network and from individual ASI-pairs are compared to the CBH-measurement of the reference ceilometer based on insightful days. Then, the coincidence of CBH, measured by ASI network and ASI-pairs with CBH measured by the ceilometer, is analyzed by scatter-density plots. Subsequently, CBH derived by the network and by all individual ASI-pairs are validated against the ceilometer by RMSD and BIAS. Finally, these deviation metrics received per interval of CBH are discussed.

4.1   Comparison of CBH measurements for two exemplary days

Figure 6 bottom visualizes time series of CBH for 02 September 2019 measured by ceilometer, by all available ASI-pairs and by the ASI network. The time series of two exemplary ASI-pairs DON-MAR and CLO-FLE with respective camera distances 0.8 and $4.2\ \mathrm{km}$ are plotted. The range of CBH-readings covered by all available ASI-pairs is shaded grey in the figure. The day features a high cirrus cloud layer which is later obscured by a low cumulus cloud layer. Occasionally, the low layer opens and the high layer is observed. Towards the evening, the sky becomes mostly clear.

In the morning (06:00), both ceilometer and the ASI network recognize adequately a high cloud layer. The ASI-pairs with valid measurements deliver similar estimations of CBH. Around (07:00), the ceilometer still recognizes the high layer whereas many ASI-pairs as well as the ASI network recognize the approaching cumulus clouds. These already cover a significant fraction of the sky in the urban area (compare Fig. 7, center). The CBH estimation approach tends to react stronger to clouds in this area of the sky in which contrasts are typically pronounced. Around 10:20 a multilayer situation is present. In the whole sky dome cumulus clouds are visible but a large fraction of the cloud cover is made up by the cirrus layer. Around this time the measurements of ceilometer and ASI network coincide well. All ASI-pairs recognize a rather low cloud layer while there are periods in which the ceilometer recognizes the cirrus layer. All of the ASI-based CBH estimations react stronger to the
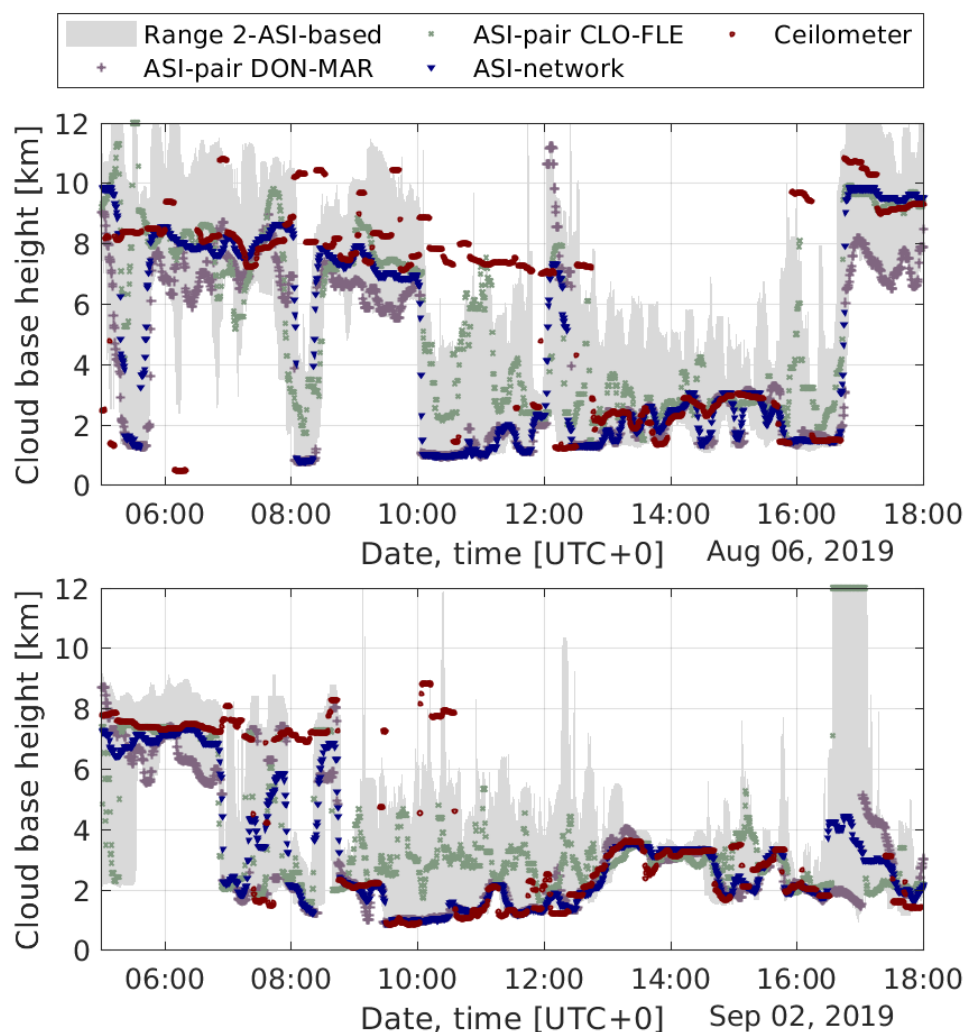
Figure 6. Time series of cloud base height for two exemplary days measured by 42 ASI-pairs (grey filled), by two exemplary ASI-pairs DON-MAR and CLO-FLE with respective camera distances 0.8 and 4.2 km, by the ASI network with refinements and by a ceilometer in the urban area of Oldenburg.

low layer and miss the high layer clouds. These two situations impress well why the ASI-based estimations of CBH are less accurate for higher clouds and tend to be negatively biased. On the other hand, for low clouds a high accuracy of the combined

375 CBH estimation is demonstrated.

Meanwhile, it is visible that, for low clouds, many ASI-pairs tend to overestimate CBH. In these conditions, the ASI network manages well to follow appropriate estimations. Around 17:00 a nearly clear sky is visible (compare Fig. 7, right). Consequently, the ceilometer does not provide any valid CBH. The ASI-pairs provide a CBH that scatters over a wide range,
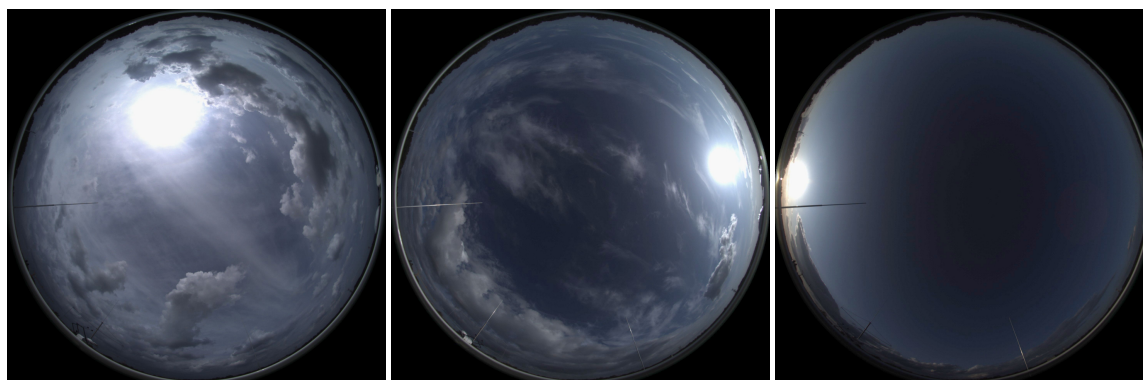
Figure 7. Sky images taken by ASI UOL representing multi-cloudlayer situations on 06 August 2019 12:35 (left) and on 02 September 2019 7:20 (center) and an almost clear-sky situation on 02 September 2019 17:00 (right) respectively.

while the ASI network provides a CBH that is assumed to be reasonable. The following CBH measurements of the ceilometer

380 around 17:30 confirm the suggested CBH of the approaching cloud layer.

Figure 6 top shows CBH on 06 August 2019 again measured by ceilometer, by all available ASI-pairs and by the ASI network. This day, similar to 02 September 2019, discussed previously, includes multi-layer conditions with high layers overlaid by low layers, resulting in similar observations. In the morning and evening high cloud layers are dominant. The CBH of these varies in the range of 7...11 km according to the ceilometer. The range of CBH from ASI-pairs reflects this spread. Still, it is

385 not obvious which of the ASI-pair based observations would be the most appropriate. From the ASI network a rather steady CBH estimation results which most of the time reflects the dominant CBH layer as recognized by the ceilometer. The combined estimation misses physically meaningful variations of CBH typically towards higher values recognized by the ceilometer. Also for this day time series of CBH and corresponding ASI images were compared. Again large underestimations of CBH by the ASI network (at 05:30, 08:15, 10:00, 12:30, 16:00) were traced back to the ASI-based estimations responding stronger to lower

390 optically denser low cloud layers which pass the vicinity of the urban area (compare Fig. 7, left).

The time series of CBH from DON-MAR and CLO-FLE demonstrate the properties of ASI-pairs with respectively small and large camera distance. DON-MAR is typically close to the reference CBH if it actually takes on a value below 4 km (e.g. 02 September 2019 9:00...13:00) while this ASI-pair tends to take on large deviations and a negative BIAS for larger CBH (e.g. 02 September 2019 6:00...9:00). ASI-pair CLO-FLE typically misses the CBH of low clouds and provides a significantly

395 overestimated CBH (e.g. 02 September 2019 9:00...13:00). For high clouds, however, CBH measured by CLO-FLE often coincides well with the reference. However, for CLO-FLE as in general for the ASI-pairs high layer clouds are missed if low layer clouds are present (e.g. 02 September 2019 6:00...9:00).
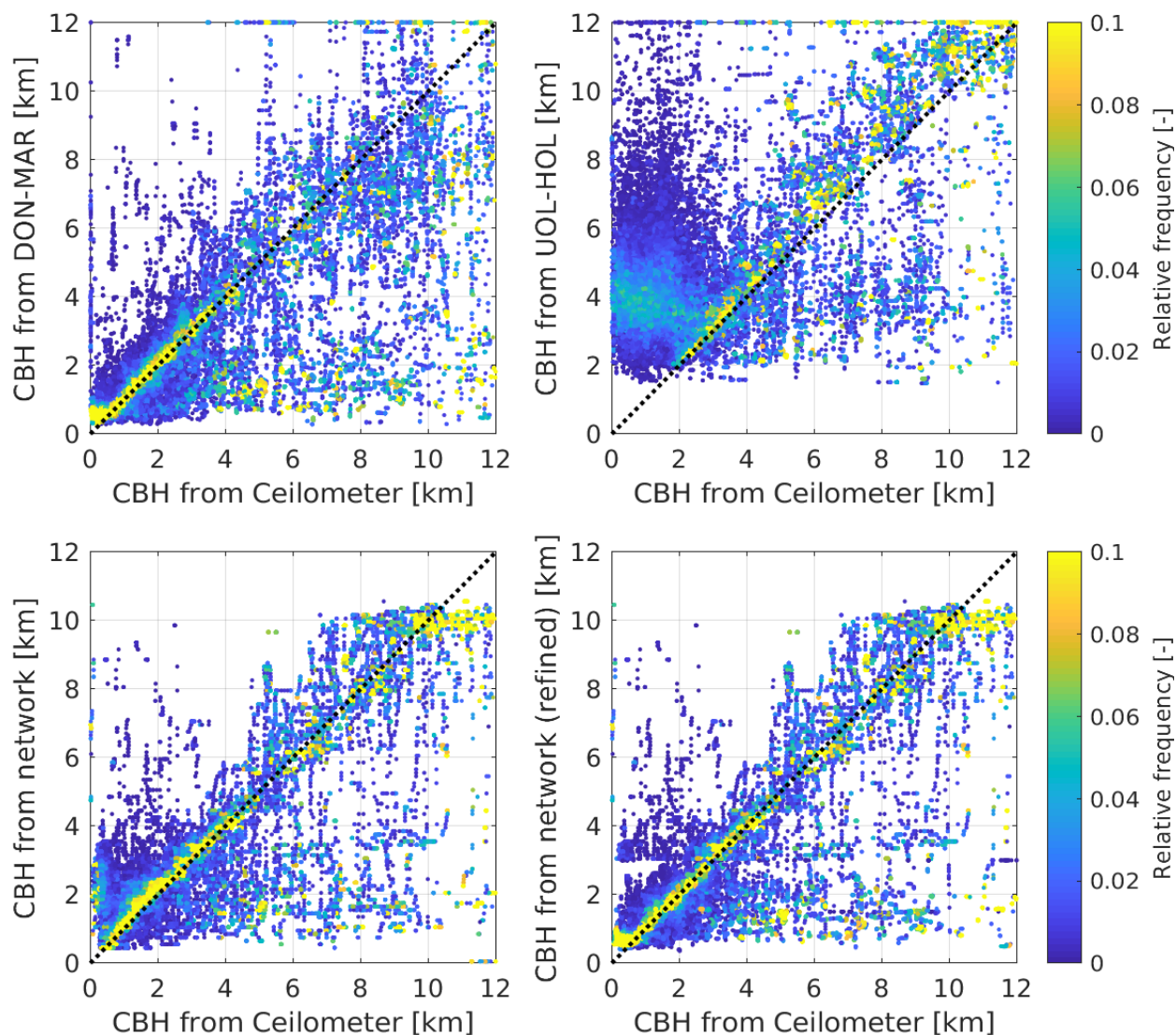
Figure 8. Relative frequency of ASI-based CBH estimation for given CBH from ceilometer, for two of the ASI-pairs DON-MAR (upper row, left) and UOL-HOL (upper row, right) with respective camera distances of 0.8 and 5.7 km, and from the ASI network without (bottom row, left) and with refinements (bottom row, right). Relative frequency in each column adds up to 1.

4.2 Comparison of CBH measurements by relative frequencies

In the following deviations found for two exemplary ASI-pairs and for the ASI network, with and without the refinements
400 described in Sect. 3.4, are analyzed with the help of scatter-density plots provided in Fig. 8. The plots visualize the relative frequency of CBH measured by the respective ASI-based systems given a CBH measured by ceilometer. Thus, relative frequencies in each of the columns add to one.

ASI-pair DON-MAR (Fig. 8 upper row, left) with camera distance 0.8 km exhibits significant scattering of the CBH readings. Additionally, CBH from the ASI-pair often deviates towards very low CBH. This feature is in part also seen for the ASI network
405 (Fig. 8 bottom row). As discussed before, this can in part result from low cloud layers which are actually present but not at the ceilometer's location. Towards high readings of the reference (≥ 8 km) DON-MAR underestimates CBH for most readings.

CBH measured by ASI-pair UOL-HOL, which has a camera distance of 5.7 km, is visualized in Fig. 8 upper row, right. CBH measured by UOL-HOL scatters randomly around a modus value of 3.8 km for reference CBH < 1.8 km. If reference CBH ranges between 1.8...3 km, this behavior is still observed for a significant part of the readings. For UOL-HOL nearly
410 no reading of less than 1.5 km is recognized. In general, strong scattering is seen for this ASI-pair. However, towards large values of reference CBH the measurement appears to scatter to a smaller extent and especially for very large CBH (> 8 km) a satisfying agreement of CBH from ASI-pair and ceilometer is seen.

The measurement of CBH by the ASI network without refinements is shown in Fig. 8 bottom row, left. The modus of the relative frequency distributions is well aligned with the main diagonal for most reference CBH. Additionally, outliers are less
415 frequent and occur with smaller deviations compared to the ASI-pairs discussed before. The ASI network returns no reading of CBH of more than 10.9 km. Thus, CBH is underestimated if a corresponding reference CBH is present. In the studied climate (see Fig. 4) and accordingly in the dataset used for modelling readings of reference CBH in this range are comparably rare. Therefore, conditional probabilities used in the estimation are modeled inaccurately. The estimation procedure uses cumulative. Compared to the usage of likelihood, this avoids frequent strong deviations resulting from these inaccuracies and yields a more
420 conservative but in this case biased estimation of CBH. For the analyzed site deviations found in this range of CBH are of minor importance. For low values of reference CBH ASI network and ASI-pair DON-MAR both appear to perform similarly at high accuracy. Only for very low values of reference CBH (especially CBH < 0.5 km) with the ASI network a large share of strong deviations is recognized. This deviation is connected to the minimum CBH which is indicated as mentioned in Sect. 4.1 for UOL-FLE but also for any other ASI-pair. Minimum CBH will be further detailed in the following section. ASI-pairs with
425 a very small minimum CBH are underrepresented in the set of available ASI-pairs: The smallest minimum CBH is provided by ASI-pairs DON-MAR and MAR-DON ranging at 0.5 km. Thus, the estimation of CBH from the ASI network is dominated by ASI-pairs which are not capable to cover the range of very small CBH.

To meet these shortcomings, refinements to the procedure have been proposed in Sect. 3.4. With these adaptions the CBH measurements shown in Fig. 8 bottom row, right are received. The adaptions noticeably affect measurements if reference CBH
430 is smaller than 3 km and most pronouncedly if reference CBH is smaller than 0.75 km. In the latter range, the ASI network

Table 1. Frequency of measurements from the validation data set (period 30 June 2019 to 27 September 2019) per range of cloud base height (CBH) used in the evaluations described in Sect. 4.

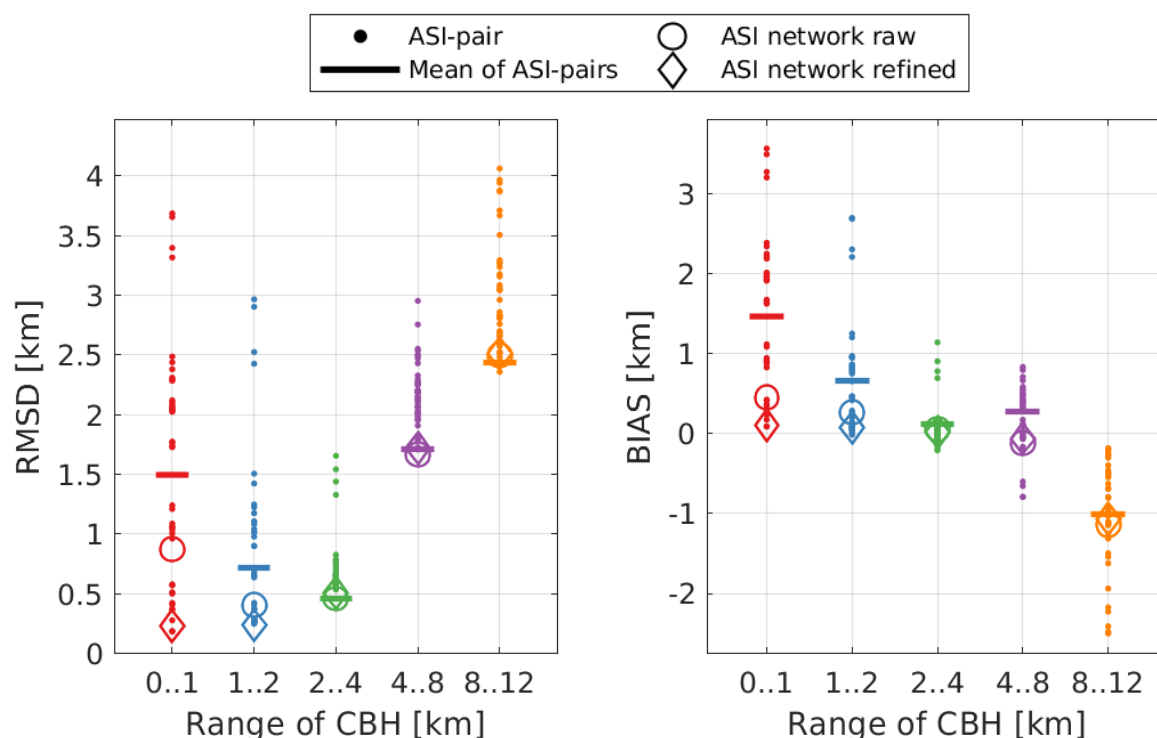| CBH range [km]	Number of observations
$0 < CBH \leq 1$	11844
$1 < CBH \leq 2$	14130
$2 < CBH \leq 4$	9962
$4 < CBH \leq 8$	5559
$8 < CBH \leq 12$	4935

Figure 9. RMSD (left) and BIAS (right) for five ranges of CBH received for all individual ASI-pairs (dots), for the ASI network without (circles), with refinements (diamonds) and for a basic average of CBH measured by all ASI-pairs (horizontal line).

behaves for the greatest part like ASI-pairs DON-MAR and MAR-DON. Concurrently, the ASI network keeps its advantages over these ASI-pairs for larger CBH as described above.

4.3 Comparison of CBH accuracy for a three-month data set

Accuracies of CBH measurement by ASI-pairs and ASI network are analyzed separately for five ranges of reference CBH

435   defined by the bounds $\{0,\ 1,\ 2,\ 4,\ 8,\ 12\}$ km. The number of CBH measurements included in this evaluation is given in Table 1 for each of these ranges. The interval bounds are spaced irregularly to correspond better to the distribution of CBH at the site (see also Fig. 4).

Figure 9 compares RMSD (left) and BIAS (right) for CBH estimated by the ASI network, with (diamonds) and without refinements (circles) described in Sect. 3.4, to all ASI-pairs (dots). As implied by the findings from Sect. 4.2 the final results

440   from the ASI network provide measurements of CBH that are the most accurate or at least among the most accurate ones for all conditions. In terms of RMSD the estimation from the ASI network is the most accurate for the range of $\text{CBH} \in [1, 8[$ km (see Fig. 9 left). For $\text{CBH} < 1$ km it is slightly outperformed by two ASI-pairs (DON-MAR, MAR-DON) as well as for $\text{CBH} > 8$ km by two other ASI-pairs (UOL-CLO, CLO-UOL). ASI network-based measurement of CBH provides among the smallest BIAS for $\text{CBH} < 8$ km (see Fig. 9 right). The magnitude of BIAS ranges constantly below 100 m. Only for

445    $\text{CBH} > 8$ km the ASI network independently from applied corrections yields a BIAS of roughly -1050 m that corresponds to the average BIAS of all used ASI-pairs for these conditions. This deviation was traced back to the ASI-based measurements of CBH missing high layer clouds in the presence of low layer clouds in Sect. 4.1. Therefore, this deviation is rather related to the different nature of the measurements (spatial-median compared to point-wise).

Figure 10 also provides deviation metrics received from the ASI network and ASI-pairs but distinguishes the latter by camera

450   distance. Metrics of the ASI network, with refinements, are given by horizontal lines. For small CBH ($\text{CBH} < 4$ km) camera distance clearly influences accuracy measured by RMSD and BIAS causing these metrics to increase steadily with camera distance. Apart from this influence metrics of the studied ASI-pairs are very similar in this range of CBH.

For intermediate and large CBH ($4...12$ km) the correlation of camera distance and accuracy is not as clear – a slight trend seen in RMSD and BIAS is overlaid by strong scattering. The variation of error metrics found between these systems

455   may indicate further influences of the setup on accuracy apart from camera distance. The lower frequency of observations of intermediate and large CBH is expected to cause a part of the observed scattering of the metrics between the various ASI-pairs. Firstly, sporadic large errors may occur only in some of the evaluated systems and dominate the received metrics for these. Secondly, from the statistics and from an inspection of the ASI images observations of higher CBH layers are likely to be found in the presence of a lower layer. As discussed in Sect. 3.1 the ASI-pairs measure CBH of the most dominant cloud layer in the

460   sense of optical thickness and area in the analyzed field of view of the sky. When for example, a CBH of 10 km is present the corresponding spatial area included has side lengths of 15.7 km. For multi-cloud-layer conditions it is likely that within this window lower clouds are present which are recognized by an ASI-pair instead. More aggressive filtering of such multilayer situations included in the evaluation could reduce this influence but would further limit the database. The distance between the cameras used by an ASI-pair and the reference ceilometer are not found to have a significant influence on received accuracy in

465   the evaluated data set. This was expected in part from the previously discussed effect that the ASI-pairs measure CBH of the most dominant cloud layer.
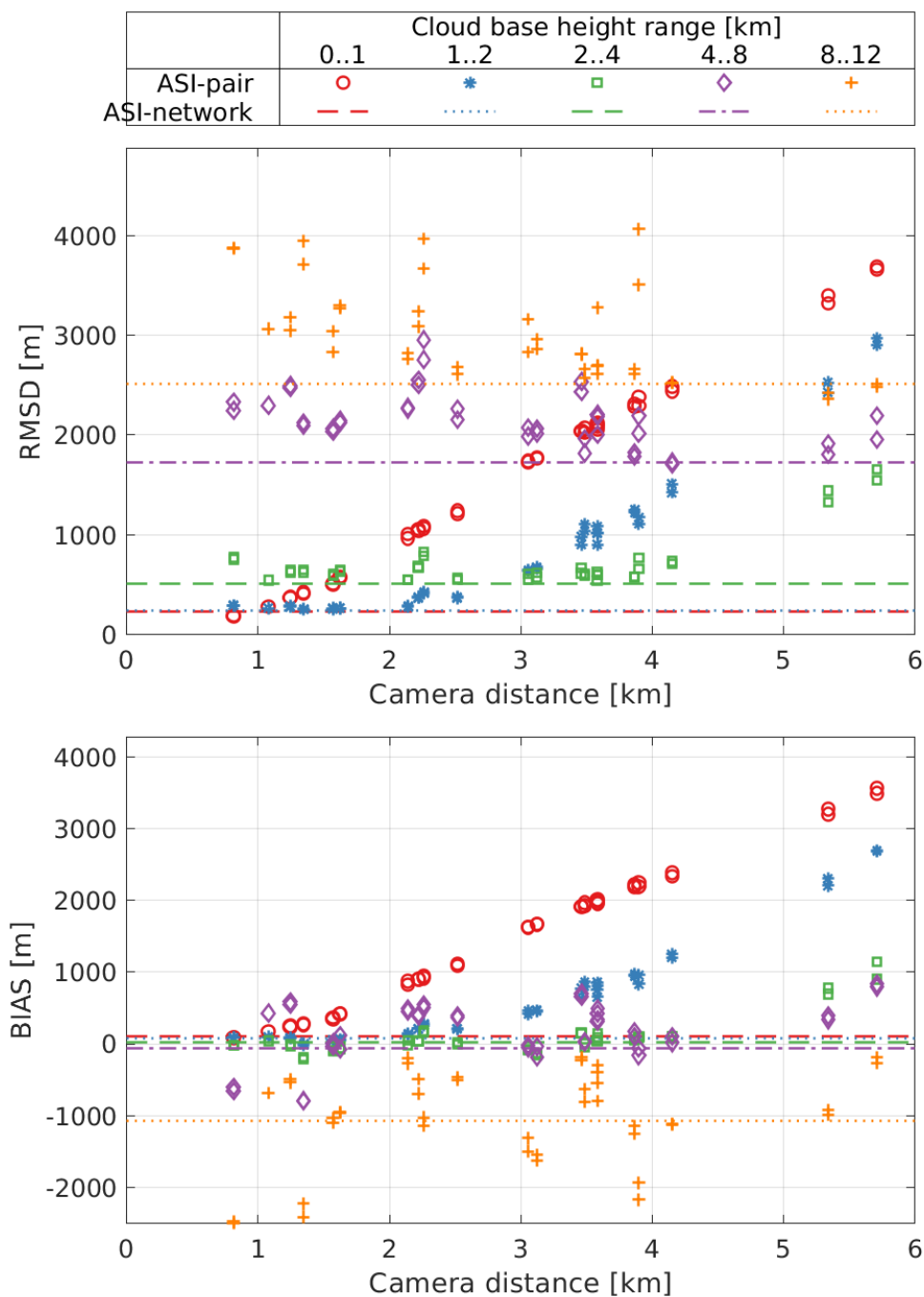
Figure 10. RMSD (top) and BIAS (bottom) received by 42 ASI-pairs utilizing camera distances in the range of 0.8...5.7 km and by the ASI network with refinements (no camera distance applicable) for the period 30 June 2019 to 27 September 2019.

Based on these findings the ASI network combines the favorable properties of the involved ASI-pairs. Over a single ASI-pair an improvement in accuracy is found as no ASI-pair can optimally cover the whole range of relevant CBH. With the achieved accuracy of the CBH measurement under all conditions at least a classification of the present cloud height is possible. CBH

470   measurement by the ASI network is found to provide a small BIAS if $CBH < 8$ km is of interest. Therefore and given the different nature of both measurements, the accuracy of CBH from the ASI network is expected to improve further if an average CBH over a range of hours is of interest.

4.4   Discussion of deviations in CBH measurement

For low CBH ($CBH < 2$ km) accuracy of the measurement by ASI-pairs decreases with camera distance. This meets the

475   expectation from Kuhn et al. (2019). Kuhn's study was limited to a maximum camera distance of 2.56 km. Additionally, the accuracy of CBH measurement was only analyzed for three ranges of CBH defined by the limits $\{0, 3, 8, 12\}$ km. We noticed that a finer classification of CBH as used in the present study yields more insights for small CBH. Figure 8 upper row provides the relative frequency of CBH readings from two exemplary ASI-pairs given a reference CBH. The camera distances of the ASI-pairs are 0.8 km (left) and 5.3 km (right) respectively. For reference CBH below a minimum value of around 2 km the

480   ASI-pair with camera distance 5.3 km in most cases provides unreasonable readings scattering around 3.8 km. For ASI-pairs with smaller camera distance a similar behavior is observed while the respective minimum CBH reduces with reduced camera distance. Accordingly, both RMSD and BIAS steadily increase with camera distance as shown in Fig. 10 for $CBH \in]0, 1[$ km. Even for the ASI-pair with camera distance 0.8 km a significant minimum CBH of 0.5 km is found (compare Fig. 8, left). In line with the discussion above for $CBH \in [1, 2[$ km both metrics only increase from a camera distance of 2.5 km on. Minimum

485   CBH of the ASI-pair for this camera distance is identified to be 1.3 km.

For intermediate and large CBH (> 4 km), increased camera distance slightly improves the accuracy of CBH estimation. On average a reduction in RMSD of 500 m is suggested over the interval of studied camera distances. No significant influence is noticed for BIAS. From Kuhn et al. (2019) the influence of camera distance on accuracy was expected to be more significant in this range of CBH. The influence of CBH on accuracy of the measurement coincides qualitatively between both studies. In

490   both cases a positive BIAS is attested for small CBH and negative BIAS for large CBH. RMSD is found to increase with CBH in absolute values. However, in the present study the magnitudes of RMSD and BIAS range well below the values found in Kuhn et al. (2019).

Beside camera distance the orientation of the camera axis to the present direction of cloud movement was considered as an influence on accuracy in Kuhn et al. (2019). Based on that study ASI-pairs may measure CBH more accurately if their

495   camera axis is aligned with the direction of cloud motion. To study this effect the direction of cloud motion was retrieved from ASI UOL as discussed in Sect. 3.2. Then the dataset was restricted to times in which clouds moved from west to east. Accuracies of ASI-pairs with similar camera distance but different orientation of the camera axis over the direction of cloud motion were compared. In this comparison no correlation of camera alignment over the direction of cloud motion and accuracy was recognized.

500   The behavior seen for CBH below a minimum value can be understood as follows. For small CBH and large camera distance the overlapping area (i.e. the fraction of the sky captured by both cameras) becomes small and corresponds to clouds located between both ASIs (Nguyen and Kleissl, 2014). These clouds are observed from very different perspectives by both ASIs. The difference in perspective may be expressed by the angular distance between a cloud's depiction in both ASIs' views. In hemispherical ASI images the similarity of a specific cloud observed by both ASIs reduces with this angular distance. Likewise,

505   the representation of two clouds, that are randomly selected from the paired ASIs' sky images respectively, will appear more similar if they are observed at a small angular distance to each other. Therefore, erroneously matched cloud edges will typically be separated by a moderate angular distance. Thus, the likelihood to match cloud objects correctly which are observed at a large angular distance by the paired ASIs is small. If actual CBH relative to camera distance is small the fraction of invalid readings (indicating not any match) increases and concurrently a large share of the valid readings goes back to mismatches. Estimated

510   cloud height scales inversely with angular distance of matched cloud patterns for stereoscopic approaches to measure CBH. Consequently, the negative bias of angular distance in the matching translates into a positive bias of estimated CBH. Except for this distinct effect the error metrics of all studied ASI-pairs are very similar for $\mathrm{CBH} < 4\,\mathrm{km}$.

Based on these findings we recommend to chose camera distance of a single ASI-pair, that is not part of an ASI network, based on the smallest CBH CBH_{min} which is of interest at a site. This consideration differs from previous studies by Nguyen

515   and Kleissl (2014) and Kuhn et al. (2019) which suggest, based on theoretical and experimental findings respectively, to optimize camera distance for the most frequent or most relevant CBH. Our experimental results suggest that camera distance of a single ASI-pair should not be chosen larger than $1.4\,\mathrm{CBH}_{min}$. For the meteorological conditions studied here ASI-pairs with even smaller camera distances than 0.8 km would be beneficial to cover the range $\mathrm{CBH} < 0.5$ km.

Figure 9 provides error metrics for the ASI network both with and without refinements described in Sect. 3.4. Without the

520   refinements, in the range $\mathrm{CBH} < 1$ km 12 ASI-pairs with camera distance up to 1.6 km perform better than the ASI network in terms of RMSD and BIAS. In this range of CBH the ASI network suffers strongly from overestimation of CBH related to the found minimum CBH of involved ASI-pairs. For sites like Oldenburg at which low cloud conditions are dominant (see Sect. 3.2) the presented approach without refinements would require a larger share of ASI-pairs with small camera distances of even less than 0.8 km. However, the refinements succeed to improve these shortcomings. Figure 9 also includes the error metrics

525   received when simply averaging CBH measurements of all ASI-pairs. The ASI network in both variants, with and without refinements, provides a significantly more accurate estimation of CBH in terms of RMSD and BIAS in most ranges of CBH compared to the simple approach.

5   Conclusions

In this study, a method was presented and benchmarked to estimate cloud base height (CBH) by a network of all-sky-imagers

530   (ASIs). The ASI network-based estimation of CBH aims to combine the measurements of CBH from ASI-pairs arranged in proximity and organized in a network. Conditional probabilities are modeled from historic CBH measurements received from ASI-pairs and a reference ceilometer. These indicate the probability that an ASI-pair with specific camera distance would

deliver a specific CBH reading if true CBH actually was in a specific range. In the inference the ASI network uses this knowledge to calculate the likeliest CBH given the readings of CBH from individual ASI-pairs. Additionally, accuracy of CBH

535 measured by 42 independent all-sky-imager (ASI)-pairs over a period of 90 days was analyzed. This validation extended prior studies of the analyzed system to the conditions of a Central-European climate (Cfb) and to an unpreceded variety of camera alignments and camera distances (0.8...5.7 km).

The influence of camera distance on the accuracy of ASI-based estimation of CBH was less pronounced than suggested by prior studies. For low clouds ($CBH < 4\,km$) small camera distances were found to lead to most accurate measurements. Under

540 these conditions deviations were found to increase steadily with camera distance as described in the literature. For higher clouds (especially for $CBH > 8\,km$) larger camera distances were found to affect received accuracy positively. However, this effect was small compared to the expectation. As main cause of deviations a minimum CBH was identified which is specific to each ASI-pair. Minimum CBH was found to increase steadily with camera distance of an ASI-pair. Below this minimum CBH ASI-pairs were found to return non-physical and positively biased readings.

545 When selecting a camera distance for an ASI-pair with stereoscopic estimation of CBH based on cross-correlation, this study suggests to consider the following depending on the meteorological conditions on-site. ASI-pairs with camera distance $< 2\,km$ are accurate only for CBH up to 4 km. ASI-pairs with camera distance $> 3\,km$ are slightly more accurate than ASI-pairs with smaller camera distance for $CBH \geq 4$ km, but much less accurate for $CBH < 4$ km than ASI-pairs with smaller camera distance. For ASI-pairs which are set up at sites with a similar distribution of CBH as in our study, we recommend including

550 camera distances smaller than 1.8 km. If mostly medium-height or high clouds are expected a greater camera distance is preferable. If possible multiple setups also including ASI-pairs with small ($< 0.8\,km$) and larger camera distances ($> 1.8\,km$) are recommended to increase accuracy for all CBH ranges. However, larger camera distances can help to increase the spatial coverage of an ASI network with a given number of cameras, which is also of advantage. A trade-off between CBH accuracy and coverage or costs must hence be found for ASI networks.

555 The presented approach to merge measurements of ASI-pairs in an ASI network combined favored properties of the individual ASI-pairs. For all five ranges, that were defined for reference CBH readings by the bin edges $0, 1, 2, 4, 8, 12$ km, the ASI network provides a measurement that is among the most accurate ones compared to individual ASI-pairs in terms of RMSD. Individual ASI-pairs slightly outperformed the network but only for single intervals of CBH. In terms of BIAS the same finding was received except for the range of $CBH \in [8, 12]$ km. In this CBH range the ASI network yields an average BIAS, compared

560 to the ASI-pairs, as all of the ASI-pairs are biased for these conditions.

The presented ASI network-based approach to CBH-measurement can be transferred to other sites using the conditional probabilities of CBH found at the Oldenburg site. Found distributions may then be extended to include more frequent observations of high clouds. Especially regarding its geometric dimensions and spatial coverage the used setup is suited for airports and large or networked solar power systems.

565 Based on the present study, the proposed approach to measure CBH in an ASI network will in future be enhanced by first extending the utilized statistics of measured CBH with data from other sites at which a combination of ASI-pair and ceilometer is available. Such an extended dataset will additionally allow to use more elaborate statistical methods including

neural networks. A procedure to generate irradiance nowcasts based on the whole ASI network utilizing the method to estimate CBH described here is under development.

Author contributions.   Investigation and conceptualization was carried out by NB. NB with contributions by BN, SW developed the methodology and software. TS, OL, JS provided used experimental resources and data curation. NB prepared the original draft and created visual-
575   izations. All authors contributed to writing, editing and review of the publication. SW, DH, AK, RPP supervised the presented work.

Competing interests.   The authors declare that they have no conflict of interest.

References

580

Aides, A., Levis, A., Holodovsky, V., Schechner, Y. Y., Althausen, D., and Vainiger, A.: Distributed Sky Imaging Radiometry and Tomography, in: IEEE Xplore/ 2020 IEEE International Conference on Computational Photography (ICCP), pp. 1–12, Saint Louis, MO, USA, 24-26 April 2020, 2020.

Allmen, M. C. and Kegelmeyer Jr, W. P.: The Computation of Cloud-Base Height from Paired Whole-Sky Imaging Cameras, Journal of
585   Atmospheric Oceanic Technology, 13, 97–113, https://doi.org/10.1175/1520-0426(1996)013<0097:TCOCBH>2.0.CO;2, 1996.

Beekmans, C., Schneider, J., Läbe, T., Lennefer, M., Stachniss, C., and Simmer, C.: Cloud photogrammetry with dense stereo for fisheye cameras, Atmospheric chemistry and physics, 16, 231–14, https://doi.org/10.5194/acp-16-14231-2016, 2016.

Bieliński, T.: A parallax shift effect correction based on cloud height for geostationary satellites and radar observations, Remote Sensing, 12, 365, https://doi.org/10.3390/rs12030365, 2020.

590 Blanc, P., Massip, P., Kazantzidis, A., Tzoumanikas, P., Kuhn, P., Wilbert, S., Schüler, D., and Prahl, C.: Short-term forecasting of high resolution local DNI maps with multiple fish-eye cameras in stereoscopic mode, AIP conference Proceedings, 1850, 140 004, https://doi.org/10.1063/1.4984512, 2017.

Blum, N., Schmidt, T., Nouri, B., Wilbert, S., Heinemann, D., Schmidt, T., Kuhn, P., Zarzalejo, L. F., and Pitz-Paal, R.: Optimierte Gruppierung verschiedener Wolkenkameras im Oldenburger Nowcasting Netzwerk, in: Tagungsunterlagen/ 34. PV-Symposium Bad Staffel-
595   stein, pp. 552–562, Bad Staffelstein, Germany, 19-21 March 2019, 2019a.

Blum, N., Schmidt, T., Nouri, B., Wilbert, S., Peerlings, E., Heinemann, D., Schmidt, T., Kuhn, P., Kazantzidis, A., Zarzalejo, L. F., and Pitz-Paal, R.: Nowcasting of Irradiance Using a Network of All-Sky-Imagers, in: EU PVSEC 2019 Proceedings/ 36th European Photovoltaic Solar Energy Conference and Exhibition, pp. 1403 – 1409, Marseille, France, 09-13 September 2019, 2019b.

Chan, K. L., Wiegner, M., Flentje, H., Mattis, I., Wagner, F., Gasteiger, J., and Geiß, A.: Evaluation of ECMWF-IFS (version 41R1) opera-
600   tional model forecasts of aerosol transport by using ceilometer network measurements, Geoscientific Model Development, 11, 3807–3831, https://doi.org/10.5194/gmd-11-3807-2018, 2018.

Cirés, E., Marcos, J., de la Parra, I., García, M., and Marroyo, L.: The potential of forecasting in reducing the LCOE in PV plants under ramp-rate restrictions, Energy, 188, 116 053, https://doi.org/10.1016/j.energy.2019.116053, 2019.

Costa-Surós, M., Calbó, J., González, J., and Martin-Vide, J.: Behavior of cloud base height from ceilometer measurements, Atmospheric
605   research, 127, 64–76, https://doi.org/10.1016/j.atmosres.2013.02.005, 2013.

Ghosh, S., Rahman, S., and Pipattanasomporn, M.: Distribution voltage regulation through active power curtailment with PV inverters and solar generation forecasts, IEEE Transactions on Sustainable Energy, 8, 13–22, https://doi.org/10.1109/TSTE.2016.2577559, 2016.

Hamann, U., Walther, A., Baum, B., Bennartz, R., Bugliaro, L., Derrien, M., Francis, P. N., Heidinger, A., Joro, S., Kniffka, A., Le Gléau, H., Lockhoff, M., Lutz, H. J., Meirink, J. F., Minnis, P., Palikonda, R., Roebeling, R., Thoss, A., Platnick, S., Watts, P., and Wind, G.: Remote
610   sensing of cloud top pressure/height from SEVIRI: analysis of ten current retrieval algorithms, Atmospheric Measurement Techniques, 7, 2839–2867, https://doi.org/10.5194/amt-7-2839-2014, 2014.

Hogan, R. J., O'Connor, E. J., and Illingworth, A. J.: Verification of cloud-fraction forecasts, Quarterly Journal of the Royal Meteorological Society: A journal of the atmospheric sciences, applied meteorology physical oceanography, 135, 1494–1511, https://doi.org/10.1002/qj.481, 2009.

615 Howie, R. M., Paxman, J., Bland, P. A., Towner, M. C., Cupak, M., Sansom, E. K., and Devillepoix, H. A.: How to build a continental scale fireball camera network, Experimental Astronomy, 43, 237–266, https://doi.org/10.1007/s10686-017-9532-7, 2017.

Atmospheric
Measurement
Techniques
Discussions

Isaac, G. A., Bailey, M., Boudala, F. S., Burrows, W. R., Cober, S. G., Crawford, R. W., Donaldson, N., Gultepe, I., Hansen, B., Heckman, I., Huang, L. X., Ling, A., Mailhot, J., Milbrandt, J. A., Reid, J., and Fournier, M.: The Canadian Airport Nowcasting System (CAN-Now), Meteorological Applications, 21, 30–49, https://doi.org/10.1002/met.1342, 2014.

620 Kaur, A., Nonnenmacher, L., Pedro, H. T., and Coimbra, C. F.: Benefits of solar forecasting for energy imbalance markets, Renewable Energy, 86, 819–830, https://doi.org/10.1016/j.renene.2015.09.011, 2016.

Khlopenkov, K., Spangenberg, D., and Smith Jr, W. L.: Fusion of Surface Ceilometer Data and Satellite Cloud Retrievals in 2D Mesh Interpolating Model with Clustering, in: Proc. SPIE 11152, Remote Sensing of Clouds and the Atmosphere XXIV/ SPIE Remote Sensing 2019, p. 111521F, Strasbourg, France, 9 October 2019, 2019.

625 Kottek, M., Grieser, J., Beck, C., Rudolf, B., and Rubel, F.: World map of the Köppen-Geiger climate classification updated, Meteorologische Zeitschrift, 15, 259–263, https://doi.org/10.1127/0941-2948/2006/0130, 2006.

Kuhn, P., Nouri, B., Wilbert, S., Prahl, C., Kozonek, N., Schmidt, T., Yasser, Z., Ramirez, L., Zarzalejo, L., and Meyer, A.: Validation of an all-sky imager–based nowcasting system for industrial PV plants, Progress in Photovoltaics: Research and Applications, 26, 608–621, https://doi.org/10.1002/pip.2968, 2018a.

630 Kuhn, P., Wirtz, M., Killius, N., Wilbert, S., Bosch, J. L., Hanrieder, N., Nouri, B., Kleissl, J., Ramirez, L., Schroedter-Homscheidt, M., Heinemann, D., Kazantzidis, A., Blanc, P., and Pitz-Paal, R.: Benchmarking three low-cost, low-maintenance cloud height measurement systems and ECMWF cloud heights against a ceilometer, Solar Energy, 168, 140–152, https://doi.org/10.1016/j.solener.2018.02.050, 2018b.

Kuhn, P., Nouri, B., Wilbert, S., Hanrieder, N., Prahl, C., Ramirez, L., Zarzalejo, L., Schmidt, T., Yasser, Z., Heinemann, D., Tzoumanikas, 635 P., Kazantzidis, A., Kleissl, J., Blanc, P., and Pitz-Paal, R.: Determination of the optimal camera distance for cloud height measurements with two all-sky imagers, Solar Energy, 179, 74–88, https://doi.org/10.1016/j.solener.2018.12.038, 2019.

Law, E. W., Prasad, A. A., Kay, M., and Taylor, R. A.: Direct normal irradiance forecasting and its application to concentrated solar thermal output forecasting–A review, Solar Energy, 108, 287–307, https://doi.org/10.1016/j.solener.2014.07.008, 2014.

Luhmann, T.: Nahbereichsphotogrammetrie: Grundlagen, Methoden und Anwendungen, Wichmann Verlag, Heidelberg, Germany, 2000.

640 Macke, A., Seifert, P., Baars, H., Barthlott, C., Beekmans, C., Behrendt, A., Bohn, B., Brueck, M., Bühl, J., and Crewell, S.: The HD (CP) 2 observational prototype experiment (HOPE)-An overview, Atmospheric chemistry and physics, 17, 4887–4914, https://doi.org/10.5194/acp-17-4887-2017, 2017.

Martucci, G., Milroy, C., and ODowd, C. D.: Detection of cloud-base height using Jenoptik CHM15K and Vaisala CL31 ceilometers, Journal of Atmospheric Oceanic Technology, 27, 305–318, https://doi.org/10.1175/2009JTECHA1326.1, 2010.

645 Mejia, F. A., Kurtz, B., Levis, A., de la Parra, Í., and Kleissl, J.: Cloud tomography applied to sky images: A virtual testbed, Solar Energy, 176, 287–300, https://doi.org/10.1016/j.solener.2018.10.023, 2018.

Nguyen, D. and Kleissl, J.: Stereographic methods for cloud base height determination using two sky imagers, Solar Energy, 107, 495–509, https://doi.org/10.1016/j.solener.2014.05.005, 2014.

Noh, Y.-J., Forsythe, J. M., Miller, S. D., Seaman, C. J., Li, Y., Heidinger, A. K., Lindsey, D. T., Rogers, M. A., and Partain, P. T.: Cloud-Base 650 Height Estimation from VIIRS. Part II: A Statistical Algorithm Based on A-Train Satellite Data, Journal of Atmospheric and Oceanic Technology, 34, 585–598, https://doi.org/10.1175/JTECH-D-16-0110.1, 2017.

Nouri, B., Kuhn, P., Wilbert, S., Prahl, C., Pitz-Paal, R., Blanc, P., Schmidt, T., Yasser, Z., Santigosa, L. R., and Heineman, D.: Nowcasting of DNI maps for the solar field based on voxel carving and individual 3D cloud objects from all sky images, AIP Conference Proceedings, 2033, 190 011, https://doi.org/10.1063/1.5067196, 2018.

655   Nouri, B., Kuhn, P., Wilbert, S., Hanrieder, N., Prahl, C., Zarzalejo, L., Kazantzidis, A., Blanc, P., and Pitz-Paal, R.: Cloud height and tracking accuracy of three all sky imager systems for individual clouds, Solar Energy, 177, 213–228, https://doi.org/10.1016/j.solener.2018.10.079, 2019a.

Nouri, B., Wilbert, S., Blum, N., Kuhn, P., Schmidt, T., Yasser, Z., Schmidt, T., Zarzalejo, L. F., Lopes, F. M., Silva, H. G., Schroedter-Homscheidt, M., Kazantzidis, A., Raeder, C., Blanc, P., and Pitz-Paal, R.: Evaluation of an All Sky Imager Based Nowcasting System for

660   Distinct Conditions and Five sites, in: solarPaces, Daegu, Korea, 1-4 October 2019, 2019b.

Nouri, B., Wilbert, S., Segura, L., Kuhn, P., Hanrieder, N., Kazantzidis, A., Schmidt, T., Zarzalejo, L., Blanc, P., and Pitz-Paal, R.: Determination of cloud transmittance for all sky imager based solar nowcasting, Solar Energy, 181, 251–263, https://doi.org/10.1016/j.solener.2019.02.004, 2019c.

Peng, Z., Yu, D., Huang, D., Heiser, J., Yoo, S., and Kalb, P.: 3D cloud detection and tracking system for solar forecast using multiple sky

665   imagers, Solar Energy, 118, 496–519, https://doi.org/10.1016/j.solener.2015.05.037, 2015.

Reynolds, D. W., Clark, D. A., Wilson, F. W., and Cook, L.: Forecast-Based Decision Support for San Francisco International Airport: A NextGen Prototype System That Improves Operations during Summer Stratus Season, Bulletin of the American Meteorological Society, 93, 1503–1518, https://doi.org/10.1175/BAMS-D-11-00038.1, 2012.

Savoy, F. M., Lemaitre, J. C., Dev, S., Lee, Y. H., and Winkler, S.: Cloud base height estimation using high-resolution whole sky imagers, in:

670   2015 IEEE International Geoscience and Remote Sensing Symposium (IGARSS), pp. 1622–1625, Milan, Italy, 26-31 July 2015, 2016.

Scaramuzza, D., Martinelli, A., and Siegwart, R.: A Toolbox for Easily Calibrating Omnidirectional Cameras, in: 2006 IEEE/ RSJ International Conference on Intelligent Robots and Systems, pp. 5695–5701, Beijing, China, 9-15 October 2006, 2006.

Schmidt, T., Kalisch, J., Lorenz, E., and Heinemann, D.: Evaluating the spatio-temporal performance of sky-imager-based solar irradiance analysis and forecasts, Atmospheric Chemistry and Physics, 16, 3399–3412, https://doi.org/10.5194/acp-16-3399-2016, 2016.

675   Schmidt, T., Heinemann, D., Vogt, T., Blum, N., Nouri, B., Wilbert, S., and Kuhn, P.: Energiemeteorologisches Wolkenkameranetzwerk für die hochaufgelöste Kurzfristprognose der solaren Einstrahlung, in: DACH-Tagung, Garmisch-Partenkirchen, Deutschland, 18-22 March 2019, 2019.

Sky cameras: https://www.solar-repository.sg/sky-cameras, last accessed: 8 July 2020, 2020.

Wang, G., Kurtz, B., and Kleissl, J.: Cloud base height from sky imager and cloud speed sensor, Solar Energy, 131, 208–221,

680   https://doi.org/10.1016/j.solener.2016.02.027, 2016.

Wessel, B., Huber, M., Wohlfart, C., Marschalk, U., Kosmann, D., and Roth, A.: Accuracy assessment of the global TanDEM-X Digital Elevation Model with GPS data, ISPRS Journal of Photogrammetry and Remote Sensing, 139, 171–182, https://doi.org/10.1016/j.isprsjprs.2018.02.017, 2018.

World Meteorological Organization, W.: Guide to meteorological instruments and methods of observation, vol. I –Measurement of Meteoro-

685   logical Variables of *WMO- No. 8*, WMO, Geneva, Switzerland, 29 edn., 2018.